Study of systematics effects on the cross power spectrum of 21 cm line and cosmic microwave background using Murchison Widefield Array data

S. Yoshiura,[1]⋆ K. Ichiki,[2,3] B. Pindor,[4,5] K. Takahashi,[1] H. Tashiro[2] and C. M. Trott[6,5,7]

[1]*Graduate School of Science and Technology, Kumamoto University, Kumamoto, 860-8555, Japan*
[2]*Department of Physics and Astrophysics, Nagoya University Furo-cho, Chikusa-ku, Nagoya, Aichi 464-8602, Japan*
[3]*Kobayashi-Maskawa Institute for the Origin of Particles and the Universe, Nagoya University Nagoya, Nagoya 464-8602, Japan*
[4]*ARC Centre of Excellence for All-sky Astrophysics (CAASTRO), Australia*
[5]*School of Physics, The University of Melbourne, Parkville, VIC 3010, Australia*
[6]*International Centre for Radio Astronomy Research, Curtin University, Bentley, WA 6102, Australia*
[7]*ARC Centre of Excellence for All Sky Astrophysics in 3 Dimensions (ASTRO 3D), Australia*

ABSTRACT

Observation of the 21 cm line signal from neutral hydrogen during the epoch of reionization is challenging due to extremely bright Galactic and extragalactic foregrounds and complicated instrumental calibration. A reasonable approach for mitigating these problems is the cross-correlation with other observables. In this work, we present the first results of the cross power spectrum (CPS) between radio images observed by the Murchison Widefield Array and the cosmic microwave background (CMB), measured by the Planck experiment. We study the systematics due to the ionospheric activity, the dependence of CPS on group of pointings, and frequency. The resulting CPS is consistent with zero because the error is dominated by the foregrounds in the 21 cm observation. Additionally, the variance of the signal indicates the presence of unexpected systematics error at small scales. Furthermore, we reduce the error by one order of magnitude with application of a foreground removal using a polynomial fitting method. Based on the results, we find that the detection of the 21 cm-CMB CPS with the MWA Phase I requires more than 99.95 per cent of the foreground signal removed, 2000 h of deep observation and 50 per cent of the sky fraction coverage.

Key words: dark ages, reionization, first stars – cosmic background radiation.

1 INTRODUCTION

At the end of the dark ages, the first stars were born in dense clouds and started to ionize neutral hydrogen (H I). As a result of the cosmological structure formation, young galaxies, and active galactic nuclei created large ionized bubbles around them. According to observations of high-z QSO spectra, almost all of the H I gas was ionized by $z \sim 6$ (Fan et al. 2006). This is the epoch of reionization (EoR) and a measurement of its precise history is a primary motivation of current observational astrophysics. There are other observations to measure the EoR. For example, the optical depth to the Thomson scattering of the cosmic microwave background (CMB) photons constrains the duration of the reionization (Planck Collaboration XLVII 2016), and the decreasing of the Lyman-α emitter luminosity function yields the neutral fraction at $z > 6$ (Ouchi et al. 2010).

In particular, the 21 cm line signal produced from the hyperfine structure of H I is a promising tool to probe the EoR. As the red-

shifted 21 cm line is observed as a function of frequency, one can measure the 21 cm line signal along the line of sight. Thus, the redshifted 21 cm line provides the three-dimensional distribution of H I gas, and we can study, for example, the nature of ionizing sources and precise history of reionization via the topology of ionized gases and its statistical property. The power spectrum is a common tool to characterize the parameters of the reionization model (e.g. Greig & Mesinger 2015).

The redshifted 21 cm line signal is observed by radio telescopes. There are many ongoing experiments, such as the Giant Metrewave Radio Telescope EoR Experiment (GMRT; Paciga et al. 2013), the Donald C. Backer Precision Array for Probing the Epoch of Reionization (PAPER; Parsons et al. 2010), the LOw Frequency ARray (LOFAR; van Haarlem et al. 2013), and the Murchison Widefield Array (MWA; Bowman et al. 2013; Tingay et al. 2013). Meanwhile, the construction of future instruments such as the Hydrogen Epoch of Reionization Array (HERA; DeBoer 2016) and the low frequency Square Kilometre Array (SKA_LOW; Mellema et al. 2013) is planned to begin in a few years. The current suite of interferometers have enough sensitivity for a statistical detection of the 21 cm line signal. Although upper limits on the 21 cm power spectrum at

various scales and redshifts have been given by many groups (e.g. Parsons et al. 2014; Ali et al. 2015; Dillon et al. 2015; Jacobs et al. 2015; Beardsley et al. 2016; Patil et al. 2017), the redshifted 21 cm line signal has not been detected yet because of the insufficient sensitivity, complicated instrumental systematics, and extremely bright foregrounds.

Typically, the foreground fluctuation is 3–4 orders of magnitude larger than the 21 cm line signal. To measure the 21 cm line signal, one has to remove the synchrotron emission from our Galaxy and extragalactic point sources with high precision. As a useful character of the synchrotron radiation, the spectrum is expected to be smooth along the frequency axis. Thus, a classical method of foreground removal is the polynomial fitting along the line of sight. Although this method could be ineffective when the foregrounds have variance on the spectra, it is simple and pretty effective in the ideal case.

In addition to the foreground removal, the cross-correlation with other observable can mitigate the contamination from the foregrounds. For instance, the distribution of Lyman-α emitter correlates with the 21 cm line signal (e.g. Lidz et al. 2009; Hutter et al. 2017) but not with the foregrounds. Thus, the foregrounds contribute to the observation as a source of error and can be statistically reduced. Although the foreground removal is required to mitigate the error (Yoshiura et al. 2017), many works show that the MWA and the SKA1_LOW have potential to detect the 21 cm-LAE cross power spectrum (CPS) (Kubota et al. 2017).

Furthermore, the cross-correlation between the 21 cm line signal and the CMB is also a useful observable. During the EoR, the peculiar motion of ionized bubbles generates the Doppler anisotropy to the scattered CMB photons. Because the 21 cm line signal distribution reflects the topology of ionized bubbles, the Doppler anisotropy and the 21 cm line signal have correlation at large scales ($l = 100$). According to the analytic formulae, the expected 21 cm-CMB signal consists of homogeneous part which is negative and in-homogeneous part which is positive. Furthermore, the CMB includes other kSZ fluctuations such as the Ostriker–Vishniac effect (Ostriker & Vishniac 1986) and patchy components (e.g. Alvarez 2016). The angular power spectrum (APS) of the fluctuations has peaks at $l > 300$, and the components can be a source of correlation with the 21 cm signal. There are many works predicting the signal and the expected signal amplitude is less than $10^4 \mu K^2$ depending on, for example, the duration and the timing of reionization (e.g. Cooray 2004; Salvaterra et al. 2005; Alvarez et al. 2006; Adshead & Furlanetto 2008; Jelić et al. 2010; Alvarez 2016; Ma et al. 2017). Simultaneously with the signal prediction, the less detectability has been shown (Tashiro et al. 2010).

In this work, we calculate the 21 cm-CMB CPS using MWA data and the CMB temperature map observed by the Planck experiment. Tashiro et al. (2010) have shown that a deep observation is required to detect the 21 cm-CMB CPS using the MWA, as is such for the auto power spectrum. However, in order to reduce the noise effectively, systematic errors have to be less than the thermal noise. Then, to find unexpected systematics, an analysis using a common data set is important before analysing a large amount of data. Thus, the primary purposes of this work are to study the foreground and systematics contamination on the CPS analysis. Additionally, we attempt to remove the foregrounds from the MWA data to mitigate the systematic error.

The structure of this paper is as follows. The MWA data and calibration are explained in Section 2. In Section 3, we introduce the 21 cm-CMB CPS and calculation methods. In Section 4, we describe our polynomial foreground removal method. In Section 5, we investigate the contamination of ionosphere, the dependence on groups of pointings and on frequency. The resulting auto and cross power spectra are shown in Section 6. In Section 7, we discuss the forecast. Finally, we summarize this work in Section 8.

2 MURCHISON WIDEFIELD ARRAY

The MWA is an interferometer constructed within the Murchison Radioastronomy Observatory in Western Australia. A tile consists of 16 dipole antennas and the effective area of antenna is about $20\,m^2$ at 150 MHz. The observable frequency range is 80–300 MHz, and instantaneous bandwidth is 30.72 MHz which is divided by 1.28 MHz coarse channels. The maximum baseline of the MWA phase 1 is about 3000 m and the maximum resolution is a few arcminutes. The MWA has huge primary beam (400 deg^2) and large side lobes. The large field of view (FoV) is an advantage of the MWA for the cross-correlation because the large FoV can reduce the cross-correlation error. Further details are written in Tingay et al. (2013). Note that, until middle of 2016, 128 tiles operated as one interferometer so-called the MWA Phase I. The MWA Phase II observation is ongoing with additional 128 tiles and different configuration of tiles.

In this work, we use the radio data observed by the MWA Phase I in 2013. The pointing centre is towards the EoR0 field centred at (RA, Dec.) $= (0\,h, -27\,deg)$, which was chosen to be sufficiently far from the Galactic Centre. The observed frequency range is 167–197 MHz and frequency channel is 40 kHz. The observation is operated around zenith for 3 h and the data consists of 90 observations with 112 s time interval for each of snapshots. During the 'drift and shift' observation, the direction of antenna pointing changes 5 times, with a change every 30 min towards the centre of the EoR0. It is worth noting that the beam shape of the MWA varies with the pointing (Beardsley et al. 2016; Pober et al. 2016).

Although radio frequency interference (RFI) in the Murchison Radioastronomy Observatory is minimal, 1.1 per cent of data are polluted (Offringa et al. 2015). Using the AOFlagger (Offringa et al. 2010), the data including the RFI are flagged and removed from each snapshot. For calibrating the data, we use the real time system (RTS; Mitchell et al. 2008; Ord et al. 2010), which is a primary calibration software pipeline for the MWA. There are many articles explaining the detail (Mitchell et al. 2008; Jacobs et al. 2016). We describe the brief method of the RTS below.

The RTS calibration technique is called 'Peeling method', based on the catalogue of apparent bright sources in southern sky and performed in visibility space. The point source catalogue of the EoR0 field is build using the Positional Update and Matching Algorithm (PUMA; Line et al. 2017). The catalogue is used in the main calibration process of the RTS, named Calibrator Measurement Loop (CML). During the CML process, first, the models visibilities of all sources are subtracted from the data. Secondly, the visibilities of the target sources are returned into the subtracted data. Then, the data are dominated by the target source, and one can measure the ionospheric offsets from a phase ramp by fitting to the visibility phased to the position of the aimed source. In this work, the ionospheric offset is corrected using 1000 point sources. Finally, five brightest sources in the catalogue are used to correct the direction-dependent antenna gains. After the calibration, the 1000 point sources are peeled from the visibility. Using the calibrated visibilities, the RTS imager provides the snapshot images with wide-field corrections.

We obtain output images at every snapshot (112 s) and coarse band channel (1.28 MHz) in the HEALpix frame (Górski et al. 2005). For reducing the thermal noise contamination, 90 observations are integrated into a main image at every ∼8 MHz, namely a
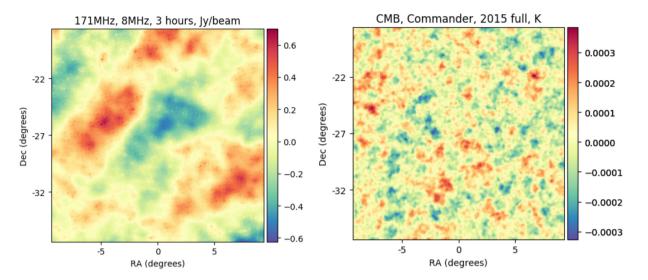
Figure 1. Left-hand panel is the observed image centred at EoR0 field, (RA, Dec.) $= (0, -27)$, with $\Delta B = 8$ MHz, $t_{\rm int} = 3$ h. The FoV is $\sim (20\,{\rm deg})^2$ and the centred frequency is 171 MHz. This image is made from 540 snapshots created by RTS with natural weights. Using the RTS, 1000 bright point sources are peeled. The image shows apparent diffuse structure and un-subtracted point sources. Negative value is a result of lack of sampling at the centre of UV-plane. Right-hand panel is the CMB temperature fluctuation map corresponding to the EoR0 field.

main image includes 540 snapshots. Left-hand panel of Fig. 1 is the image centred at 171 MHz using natural weighting. This image is almost consistent with the fig. 8 in Beardsley et al. (2016) except the size and resolution. There is apparent diffuse emission and un-subtracted point sources. Note that the lack of visibility at $(u, v) = (0, 0)$ (no autocorrelations) causes the negative values, whereby a constant sky temperature cannot be reconstructed.

In addition to the images, the calibrated visibility data are an output of the RTS. In this work, we take the average of the visibilities in the UV-plane with $\Delta u = 1$ at every coarse band channel. These gridded visibilities are used to calculate the APS.

3 METHODS

In this section, we describe the method to calculate the APS, CPS, and the error of the CPS.

3.1 Angular power spectrum

The APS is defined as ensemble average of spherical harmonics expansion coefficients,

$$\langle a_{lm} a^*_{l'm'} \rangle = \delta_{ll'} \delta_{mm'} \langle C_l \rangle, \tag{1}$$

where $\delta_{ii'}$ is Kronecker symbol and,

$$a_{lm}(\nu) = \int {\rm d}\Omega \, Y^*_{lm} \, I(\nu, \theta). \tag{2}$$

Here $I(\nu, \boldsymbol{\theta})$ is intensity of the images.

To calculate the APS from images, we use Polspice[1] (Chon et al. 2004), which is originally developed for estimating the CMB polarization power spectrum. The APS is evaluated via weighted correlation function of images, and full method is described in Chon et al. (2004). The Polspice has been used in some literatures such as the BICEP 2 yr data analysis (Chiang et al. 2010), the CMBPol mission concept study (Dunkley et al. 2009), and the angular power spectra

[1] http://www2.iap.fr/users/hivon/software/PolSpice/

of the Planck frequency maps (Planck Collaboration XI 2016). Note that an image created from visibility has weight effect caused from the UV-coverage. For correct estimation of APS, we have to correct the weight. The correction method is described in the Appendix.

The units of the images made by using the RTS is Jy beam^{-1}, and we need to convert Jy beam^{-1} into K. However, the conversion is not straightforward because it needs an accurate beam model. Thus, in this work, we normalize the APS of the images using a constant factor so that the image APS is consistent with the APS calculated from the visibilities at $\ell = 500$.

The APS of visibility data is computed as (Trott, Wayth & Tingay 2012),

$$C_l = \frac{\sum\limits_{2\pi|u|=l} N_{\rm UV} |V_{\rm UV}|^2}{\sum\limits_{2\pi|u|=l} N_{\rm UV}}, \tag{3}$$

where $N_{\rm UV}$ is the number of visibility samples at a UV-grid and $V_{\rm UV}$ is the averaged visibility. The units of visibility is Jy, and we convert Jy into K as

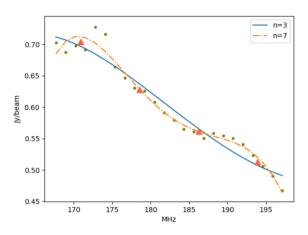$$K = \frac{\lambda^2}{2 \times 10^{26} k_{\rm B} \Omega} ({\rm Jy}) \tag{4}$$

where λ is observed wavelength, $k_{\rm B}$ is the Boltzmann constant, and Ω is the solid angle of the MWA's field-of-view.

The APS using the visibility data can be used to estimate the error power of the 21 cm observation. For the error estimation, we split the data into 'even' and 'odd' samplings at 8 s time intervals, and calculate the APS of the difference between the samplings. Ideally, the 21 cm signal and the foreground radiation are common in those two groups while the thermal noise is time variant. Therefore, the difference should be dominated by the thermal noise.

3.2 Cross power spectrum

Using the Polspice, we calculate the CPS from images of the MWA radio map and the CMB temperature fluctuation map. The definition
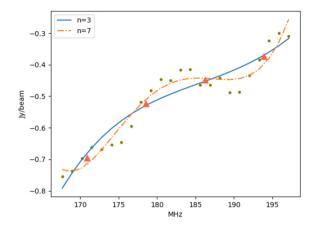
Figure 2. Examples of foreground fitting along the line of sight. Left-hand and right-hand panels show the case of the brightest pixel and the faintest pixel at $\nu = 167$ MHz. The green circles are values of the images with 1.28 MHz as ΔB, and the orange triangles are values of the pixels from images with 8 MHz bandwidth. The solid, dashed, and dot–dashed lines are obtained by fitting to 24 circles with $n = 3$ and 7.

is written as

$$\langle a_{lm}^{21} a_{l'm'}^{\mathrm{CMB},*} \rangle = \delta_{ll'} \delta_{mm'} \langle C_l^{21,\mathrm{CMB}} \rangle, \tag{5}$$

where a_{lm}^{21} and a_{lm}^{CMB} are calculated from the MWA image and the CMB image. The images are cut into square of 20×20 deg^2 and the masked field could be a unique response on the signal. The mask effect is reduced using the Polspice (Chon et al. 2004). Same as the APS, we correct the weight caused from incomplete UV-coverage.

The CPS should be computed from the visibility to account for UV-coverage and avoid the systematics caused from imaging. For the calculation, one has to Fourier Transform the CMB image into the visibility UV-plane. In this work, the CPS is calculated from images because we remove foreground using the line-of-sight fitting method. Computation via visibilities is left for future work.

The error of CPS is estimated using (Knox 1995)

$$\Delta C_l^2 = A \left[\left(C_l^{21,\mathrm{CMB}} \right)^2 + \left(C_l^{21,\mathrm{obs}} \right) \left(C_l^{\mathrm{CMB,obs}} \right) \right],$$
$$= A \left[\left(C_l^{21,\mathrm{CMB}} \right)^2 + \left(C_l^{21} + N_l^{21} + C_l^{\mathrm{FG}} \right) \left(C_l^{\mathrm{CMB}} + N_l^{\mathrm{CMB}} \right) \right], \tag{6}$$

where $A^{-1} = (2l + 1) f_{\mathrm{sky}} \Delta l$, f_{sky} is the sky fraction of the image, Δl is the bin width, $C_l^{\mathrm{MWA,obs}}$ is the APS of the images observed by the MWA, and $C_l^{\mathrm{CMB,obs}}$ is the APS of the CMB image. The error consists of a sample variance term and a contribution of 21 cm APS, noise of the 21 cm observation, foreground APS, the CMB APS, and the noise of the CMB observation. In this work, we ignore the error term of the sample variance, which should be smaller than other terms. In practice, the CMB temperature map includes the foreground residual, which can correlate with the foreground of the 21 cm observation. However, the foreground contamination is sufficiently smaller than the CMB signal, and therefore we ignore this term. In addition, we consider the error propagation as described in the Appendix because we use the weighted CPS.

For the calculation, we use the 2015 CMB full mission Commander map stored in Planck Legacy Archive.[2] The right-hand panel of Fig. 1 shows the CMB map associated with the EoR0 field.

4 FOREGROUND REMOVAL

As shown in equation (6), the foregrounds contribute to 21 cm-CMB CPS as a source of error. Since the foregrounds are a few orders of magnitude brighter than other contributions, the terms of the foreground and CMB PS dominate the total error. Thus, one has to remove the foreground from the MWA images. Although 1000 bright point sources have been subtracted from the MWA data, the diffuse emission and un-peeled sources remain in the data. In this work, we perform a simple polynomial fitting to the spectral dimension of the data, and use this as the foreground removal.

First, we make 24 images with 1.28 MHz spectral channels from the MWA data in the observed frequency range of 167–197 MHz. Next, we fit a nth-order polynomial function along the frequency axis at each pixel of the image cube, and obtain smooth functions. Finally, we subtract the smooth functions from our main images.

The left-hand (right-hand) panel of Fig. 2 shows examples of the fitting for the brightest (faintest) pixel at 167 MHz. Circles are values at a pixel of each image for the fitting, and triangles are values of main images. Clearly, the circles are not smooth and have a wave-like feature as a function of frequency. This feature is caused from the mode-mixing and frequency dependence of the instrumental point spread function (e.g. Morales et al. 2012). In the images transformed from visibility data, there is a concentric side lobe structure around point sources because of the sparse UV-coverage, and the side lobe propagates emission from point sources in the field. Perfect removal of this structure is impossible due to the number of point sources.

In the panels, the fitting function with $n = 3$ does not reproduce the data and a higher nth-order polynomial function is required.[3] Thus, the remaining signal could be corrupted by the foreground residuals. In order to reduce the residual contamination, we attempt to fit with $n = 7$ and the reproduction of the data is better than $n = 3$. However, the 7th polynomial fitting slightly improves the results discussed following section. Thus, we adopt $n = 7$ for the foreground removal in this work. Note that the higher order polynomial fitting function could fit out the EoR signal.

[3]Since the diffuse emission should be spectrally smooth, the polynomial fitting method is effective. However, to remove the point source contribution which is the wave-like spectrum, we may need additional functions.
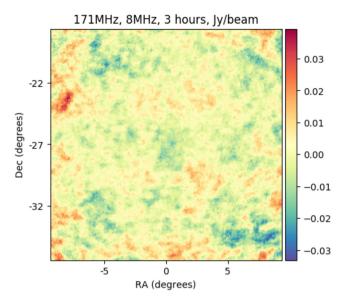
Figure 3. The EoR0 field at 171 MHz with $\Delta B = 8$ MHz, $t_{int} = 3$ h, $(20 \deg)^2$. We remove the foregrounds by the polynomial fitting with $n = 7$ to the image shown in Fig. 1. The large-scale features have been removed and the fluctuation is reduced by one order of magnitude.

Generally, the expected spectral index of the synchrotron emission is negative. However, as shown in the right-hand panel of Fig. 2, the data show a positive index, which is understood as below. The average intensity is subtracted from actual intensity since the interferometer cannot observe the visibility at $(u, v) = (0, 0)$. Then, for example, the intensity of image is $F(\nu, \theta) - F_{ave}(\nu)$, where true flux of a LOS is $F(\nu, \theta) = F_0 \nu^{\alpha}$ and averaged flux is $F_{ave}(\nu) = F_{ave,0} \nu^{\overline{\alpha}}$. If the index α is larger than the $\overline{\alpha}$, the index of observed intensity can be positive.

Fig. 3 shows the image at 171 MHz after performing the polynomial foreground removal with $n = 3$. Interestingly, although the foreground removal method is relatively simple and has no prior that uses spatial correlation, we can reduce the diffuse structure shown in the left-hand panel of Fig. 1 and reduce the fluctuation by one order of magnitude.

The quality of fitting depends on regions because the smoothness is different for each LOS. In this work, we quantify the quality of the fitting using squared error, $\sum_i (d_i - f_i)^2$, where i denotes the number of frequency bins, d_i denotes the data, and f_i is the fitting function. Fig. 4 shows the distribution of the error, and the spectral fitting works well in the centre of the region. Thus, we calculate the APS using a region centred at (RA, Dec.) $= (-0.133$ h, -28 deg) with a 4 deg radius, and then the resulting APS is reduced by 2 times. However, we do not use the mask for simplicity and reducing the error of CPS which is proportional to $f_{sky}^{-0.5}$.

5 ADDRESSING SYSTEMATICS

21 cm observations with interferometers suffer from systematics such as refraction due to electrons in the Earth's ionosphere, instrumental systematics, and intrinsic foreground spectra. Thus, a better understanding about the systematics of the data is worthwhile for future further analysis. In this section, we study the effect of ionosphere, pointing of observation, and frequency dependence of the CPS by comparing with that of the APS.
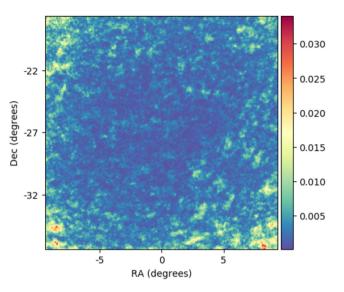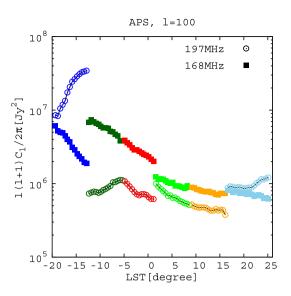

Figure 4. The squared error of the polynomial foreground removal with $n = 7$. In the centre of EoR0 field, the polynomial fitting works properly.

5.1 Pointing dependence

The MWA observation is 3 h continuous observation around zenith, and the signal can be calculated as a function of the Local Sidereal Time (LST). Furthermore, the observation strategy is the drift and shift observation, and the direction of pointing changes 5 times towards the centre of the EoR0 field. Fig. 5 shows the LST dependence of the APS calculated from 90 visibility data sets. The colours represent the group of pointing. The right-hand panel shows that the APS at 168 MHz is larger than the APS at 197 MHz on the small scale. On the other hand, as shown in the left-hand panel, the APS at 197 MHz exceeds the APS at 168 MHz in range of LST < -13 and LST > 16 on large scale. During observation with these LST, the pointing is off-zenith and then the MWA has large side lobes (e.g. Neben et al. 2015). Furthermore, the gain of the side lobe is high at high frequency, and the second side lobe is close to the Galactic centre. Thus, the enhancement of the APS at 197 MHz on large scale shows the leakage of the Galactic synchrotron emission. The top left panel of Fig. 6 shows the LST dependence of the absolute CPS at $l = 100$. As is the case for the APS, the CPS increases at LST < -13 deg where the APS has serious foreground contamination, and the CPS at 197 MHz is larger than the CPS at 168 MHz. The LST dependence is apparent in the bottom left panel, which shows the CPS in linear scale. Apart from foreground contamination at LST < -13 deg, the amplitude of CPS 167 MHz is larger than the CPS at 197 MHz, and CPS oscillates around zero. These results indicate that the CPS is dominated by errors due to foregrounds, which should be proportional to $(C_l^{FG})^{1/2}$. Same as left-hand panels, blue circles indicate the foreground contamination on the CPS at $l = 500$ in the bottom right panel of Fig. 6.

5.2 Ionosphere dependence

The Earth's ionosphere refracts radio waves and produces phase errors and spatial offsets of radio point sources in interferometer measurements. Although the RTS calibrates the phase error, the uncalibrated error can produce residuals of point sources after the point source subtraction. Here, we show the effect of ionosphere activity on the APS and CPS.
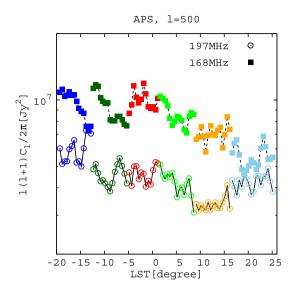
Figure 5. The LST dependence of APS at $l = 100$ and $l = 500$. Each points are the APS of visibility data with $\Delta B = 1.28$ MHz and $t_{int} = 112$ s. Colours indicate different group of pointing. Because the spectral index of foreground is negative, the APSs of higher frequencies are smaller than that of lower frequencies. However, the APS of 197 MHz exceeds that of 168 MHz at large scales. This is due to the Galactic emission, which leaks to the data at the lowest LST because the MWA side lobe moves towards Galactic centre and have large gain at high frequency.

In Jordan et al. (2017), they have discussed particular types of ionosphere activity by defining the metric of ionosphere quality, m, based on the total offsets of point sources and dominant eigenvalue determined by a principal component analysis to the source offsets. In general, the quiet ionosphere has $m < 4$ and the active has $m > 10$. Since, for example, the calibration error due to the ionosphere can generate the error of the point sources subtraction, then we might find a correlation of the metric value with the APS and the CPS. The metric is measured every 2 min observation, and the metric of 63 observations, used in this work, is known.

In Fig. 7, we show the ionosphere metric dependence of the APS at 167.675 and 197.115 MHz, and at $l = 100$ and 500. The colour of dots represents pointing of observation as with the Fig. 5. The metric of ionosphere does not have apparent correlation even with active ionosphere, $m > 10$. Furthermore, APS with quiet ionosphere, $m < 4$, and moderate, $4 < m < 10$, do not have particular dependence on m. This indicates that contamination due to ionosphere is smaller than the foreground residuals such as fainter point sources and diffuse foregrounds. On the other hand, pointing is a crucial systematic on the APS. As shown in right-hand panels, the blue dots are stronger than others which is also indicated from Fig. 5.

In addition, the ionosphere effect on the CPS is shown in Fig. 8, and also there is no apparent correlation between CPS and m. In the plot, we show the averaged CPS of quiet, moderate, and active ionospheres with the standard deviation as error bars. The averaged CPS with quiet and moderate ionospheres are fairly consistent with zero, but the CPS with active ionosphere is not. Thus, the ionosphere might affect the CPS, but there are only a few samples observed in the same group of pointings. Furthermore, same as Fig. 7, the dependency on sets of pointings can be found in the top right panel of Fig. 8. This shows the contamination of leaked foreground on the error of CPS. Before moving to the next analysis, it is worth noting that the CPS oscillates around zero in Fig. 8. This indicates that the CPS is dominated by the error including thermal noise and foreground.

Systematics due to the ionosphere should be more important at smaller scales. However, we also do not find any correlation at

$l = 1000$ (not shown in this work) just as for $l = 100$ and $l = 500$. We note that only two of our samples have an active ionosphere, and an analysis with a more representative sample of ionospheric conditions will be required to more fully investigate these effects. We leave this for future work.

5.3 Frequency dependence

The APS and CPS are expected to be dominated by the foregrounds, which depend on frequency. Here, we show the frequency dependence of the MWA data.

Fig. 9 shows the APS calculated from visibility data with 1.28 MHz bandwidth in units of Jy^2. At small scale ($l > 200$), the signal increases with decreasing frequency, and the APS at 167 MHz is 1.53 times larger than the signal at 197 MHz. This feature is consistent with the negative spectral index of point source foregrounds (e.g. Hurley-Walker et al. 2017). On the other hand, at large scales, the several APSs at high frequencies are stronger than that of low-frequency data. As discussed above, the APS is dominated by the Galactic synchrotron emission with the negative spectral index at these scales, and therefore this feature is un-expected. This feature is caused from the pointing dependence of APS as shown in Fig. 5.

Frequency dependence of the CPS is shown in the Fig. 10. No clear tendency can be seen in the behaviour of the CPS. However, the CPS is dominated by foreground error, as indicated in the above analysis (e.g. Figs 8 and 6). Thus, Fig. 10 indicates that the frequency dependence is weaker than the variance due to foreground errors. However, the CPS shows weak oscillation and frequency dependence at $l < 300$. This result suggests that the CPS has only a few independent modes at large scales and the modes do not vary with frequency. Furthermore, at $l > 1200$, the CPS is always positive, and this indicates unexpected systematics at small scales.

6 RESULTS

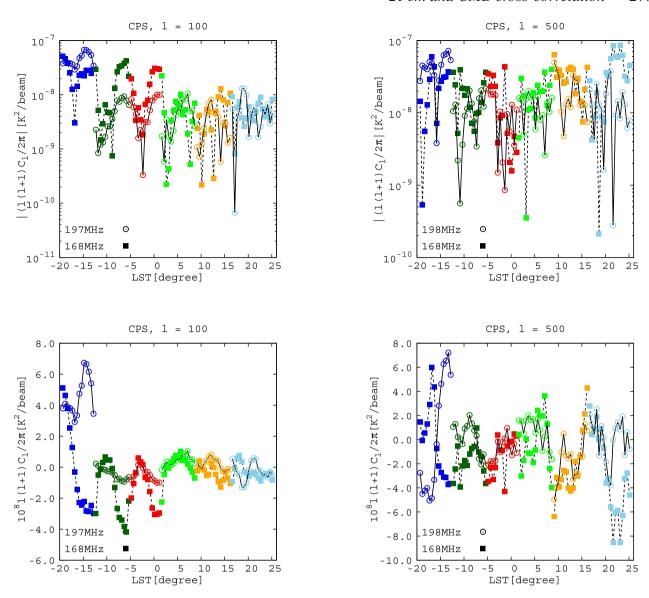In this section, we discuss the APS and CPS from the MWA data and the Planck CMB map after 3 h integration.

Figure 6. The LST dependence of CPS at $l = 100$ and $l = 500$. Each points are the CPS of image data with $\Delta B = 1.28$ MHz and $t_{int} = 112$ s. Same as Fig. 5, Colours indicate different group of pointing. Top panels show the absolute value of CPS, and bottom panels show the CPS in linear scale.

6.1 Angular power spectrum

To understand the MWA data, we calculate the APS using different five data sets. The five data sets are: (i) the visibility with no source peeling, (ii) visibility with peeling of 1000 sources, (iii) image with peeling of 1000 sources, (iv) image with the polynomial foreground removal and peeling of 1000 sources, and (v) visibility of the thermal noise. Fig. 11 compares the resulting APS at $\nu = 167, 176, 186,$ and 194 MHz.

The APS using visibilities without peeling increases with l and overwhelms the APS with peeling of 1000 sources at all scales. Thus, the apparent 1000 point sources dominate the signal. Meanwhile, the APS calculated from visibility with peeling shows a flat slope at large scales and rises at small scales. This different index can be understood as that the point source foregrounds dominate at small scales and the diffuse Galactic emission is powerful at large scales. Typically, the expected 21 cm APS is less than $10^{-4}(K^2)$ at $\ell = 100$ (Datta, Choudhury & Bharadwaj 2007), and therefore we

have to reduce the foregrounds by at least six orders of magnitude in K^2 to measure the 21 cm line signal.

The noise APS of the MWA observation is sufficiently smaller than the measured signal dominated by the foreground. However, the noise is larger than the expected 21 cm line signal. Thus, in addition to the precise foreground removal, we need a deep integration in time for the measurement of 21 cm line signal.

The APS calculated from image with peeling 1000 sources should be consistent with the APS of the visibility since these data have the calibration and the point source subtraction in common. Indeed, the Fig. 11 shows that the APS of image is fairly consistent with the APS of visibility. However, the APS of image is smaller than the APS of visibility at $\ell = 25$. This could be because that the APS of visibility is enhanced by the primary beam shape of the MWA (e.g. fig. 1 in Trott et al. 2016) but the weight of mask can be corrected in the APS of images by using Polspice.

By using the polynomial fitting, we can reduce the foreground contamination in the APS. If the foreground removal is accurate,
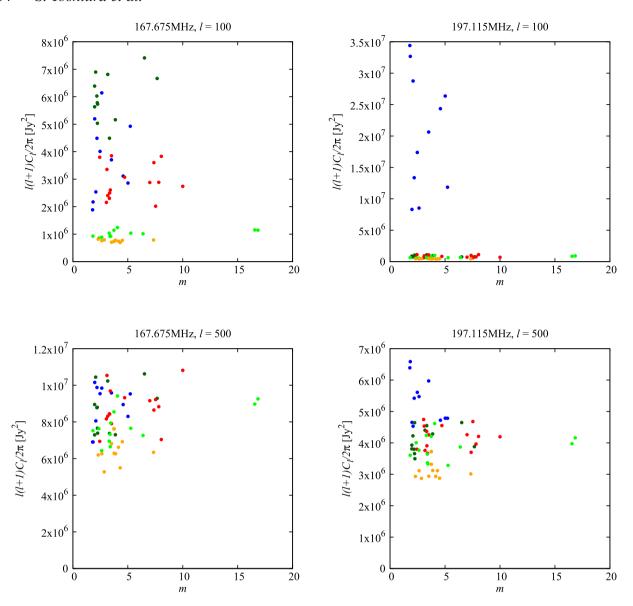
Figure 7. Ionosphere activity dependence of APS at $l = 100$ (top) and 500 (bottom). We show the APS at 167.675 and 197.115 MHz in left-hand and right-hand panels. Each dots are the APS of image data with $\Delta B = 1.28$ MHz and $t_{int} = 112$ s. Same as Fig. 5, different colour shows different group of pointings.

the resulting APS should be consistent with the thermal noise contamination. However, the APS of the foreground removed image is larger than the noise level since our simple foreground removal is not perfect. Nevertheless, the APS of the foreground removed image is three orders of magnitude smaller than the APS with peeling of 1000 sources at $l = 100$. Furthermore, the APS is reduced 1–2 orders of magnitude at small scales. This indicates that the polynomial fitting removes both the diffuse emission and the point sources. However, the remaining signal is larger than the expected signal. Thus, other accurate foreground removal is required to remove the foreground residuals.

It should be noted that the APS with the foreground removal is smaller than the noise level at small scales. This unexpected result could be caused from overfitting. At the small scales, the thermal noise is 10 per cent of total signal and then the thermal noise could be fitted by the polynomial function.

We compute the APS of the foreground model obtained using the polynomial fitting. Fig. 12 shows that the APS of the fore-

ground model is consistent with the APS of the main image at 171 MHz. The amplitude of the difference is larger than the APS of the residual image at large scales. This is indicative of the variance due to the cross term of the foreground model and the residual.

6.2 21 cm-CMB cross power spectrum

Fig. 13 shows the resulting CPS at each frequency without the polynomial foreground removal, with the 1σ and 3σ error estimated using equation (6), where $\Delta l = 100$. There is no-detection of any signal at $l < 1000$ within a 3σ error. Circles and squares represent the negative and positive sign, and the change of sign is a result of large error dominated by the foregrounds. Also, this indicates that there is not strong systematics such as the correlation between the foregrounds of the 21 cm observation and the foreground residual in the CMB data. The expected 21 cm-CMB CPS has a peak at $l = 100$, and we obtain $3 \times 10^7 \mu K^2$ as the 1σ error on the scale.
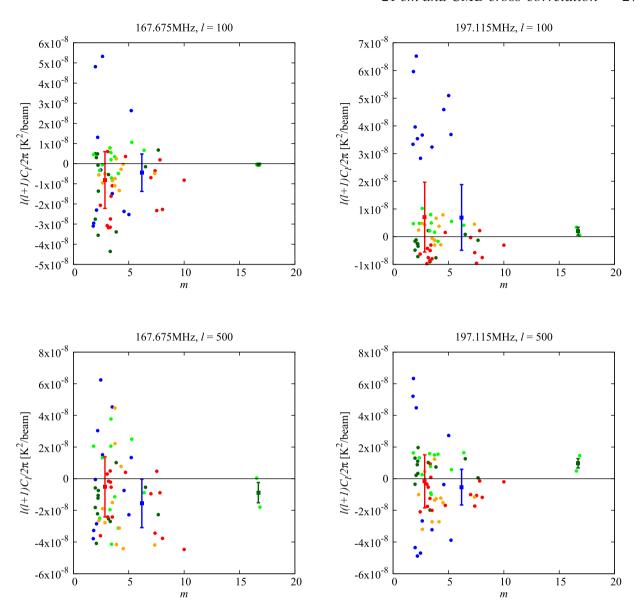
Figure 8. Same as Fig. 7, but for the CPS. Red, blue, and green squares and error bars show average value and standard deviation of CPS with quiet, moderate, and active ionospheres, respectively.

Table 1 lists the measured signal and error at different scales and frequencies.

The foreground emission is expected to be weak at high frequency due to the negative spectral index of synchrotron emission. As anticipated, the error and the amplitude of the measured signal are large at low frequency on large scales. We note that the signal is contaminated by large variance.

At $l > 1000$, we find detection of an unexpected signal with 2–3σ significance, especially at 194 MHz. However, at these scales, the foreground residual of the CMB is small and therefore the correlation of foregrounds is unlikely to be the source of the detection. Thus, this detection suggests that we underestimate the error on the CPS since the equation (6) is valid only if the error follows a Gaussian distribution.

In order to evaluate the error numerically, we attempt to calculate the CPS between the MWA image and 100 different CMB images. Fig. 14 shows comparison between the variance of signals and the error estimated by the equation (6) at 194 MHz. The variance is con-

sistently larger than the expected error at $l > 200$. This indicates an additional contamination to the error term, such as a non-Gaussian error and unexpected systematics. This error could caused from the point sources which dominates the APS at the scales. On the other hand, the variance is fairly consistent with the expected error at $l \approx 100$. This indicates that the systematics is small on large scales. Note that the variance is a conditional error since we fix the MWA image. Thus, we use the error of equation (6) for the analysis.

The Fig. 15 shows the results with images using the polynomial foreground removal. At all scales, there is no significant detection and the error dominates the signal. However, the CPS and the error are reduced to one order of magnitude weaker than that of Fig. 13. We mention that our foreground removal method is simple and this method can provide critical signal loss and un-expected systematics especially at small scales ($l > 1000$) as shown in the Fig. 11. In Table 2, we summaries the measured values and the 1σ error.

Same as Fig. 14, we compare the variance with error and find that the variance of the CPS with the polynomial foreground removal is
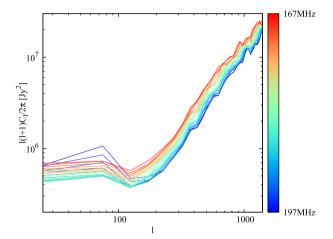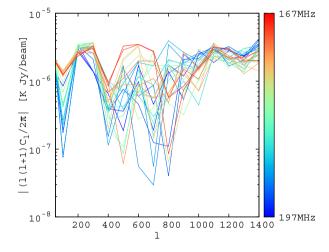
Figure 9. The APS computed from visibility data with 1.28 MHz bandwidth. The redder line shows the low-frequency data and the bluer shows high frequency. At small scales, the high-frequency APS is smaller than the low-frequency APS. However, some of APS at high frequency enhanced at large scales. This is caused by the leakage of Galactic synchrotron emission from the side lobe.
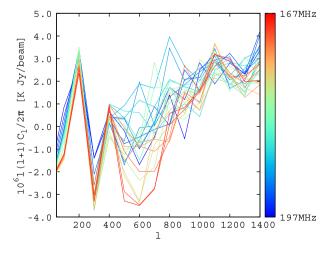

Figure 10. Same as Fig. 9, but for the CPS calculated from images. We show the absolute value in top panel, and the bottom panel shows the signal in linear scale.

consistent with the estimated error at all scales. This indicates that unexpected systematic error is likely due to the foregrounds.

7 FORECAST

We discuss the feasibility of measuring the 21 cm-CMB CPS based on the results. Previous works predict that the signal has peak at $l = 100$. For example, Alvarez et al. (2006) showed the CPS between 21 cm signal and Doppler anisotropy is $-200\,\mu K^2$ at $z = 7.5$. However, the correlation between 21 cm signal and CMB anisotropy is caused from not only the Doppler effect but also Ostriker–Vishniac (OV) effects and patchy reionization (e.g. Alvarez 2016). We mention that the fluctuation due to the Doppler effect dominates the kSZ anisotropy at large scale $l < 100$, and the patchy and the OV anisotropy contribute at $l > 200$. Furthermore, the amplitude strongly depends on the reionization model, and therefore we assume the 21 cm-CMB CPS is $10^3\,\mu K^2$ at the scale as an optimistic prediction.

The error is $3 \times 10^7\,\mu K^2$ for the data with peeling of 1000 point sources, and therefore the expected signal-to-noise ratio (SNR) of the result is 3.3×10^{-5}. The foreground removal of the polynomial fitting reduces the error and the SNR is 10^{-3}.

Using the noise APS and equation (6), we can estimate the SNR under the assumption that we have a perfect foreground removal. At $l = 100$, the noise APS and the CMB APS are $10^{10}\,\mu K^2$ and $3000\,\mu K^2$. Thus, the error term of the thermal noise and the CMB APS is $4 \times 10^5\,\mu K^2$. Although the noise contribution is smaller than the foreground contamination, the expected signal is 400 times smaller than the error caused by the thermal noise.

In order to increase the SNR, precise foreground removal and deep observations are required. Also, a large FoV can reduce the error of the 21 cm-CMB CPS, which is proportional to $f_{sky}^{-0.5}$. Fig. 16 shows the contour of the expected SNR at $l = 100$ in the observation time and the sky fraction plane. The SNR at $f_{sky} = 0.01$ and $t_{obs} = 3\,h$ corresponds to the SNR of this work. In the left-hand panel, we assume the foreground is perfectly removed. To achieve the SNR ≈ 1, the MWA needs 2000 h of observation for each MWA FoV and 50 per cent of sky fraction, but such enormous survey is not realistic. Thus, more sensitive instruments are necessary for the measurement. Fortunately, the MWA Phase II has additional tiles which form two hexagonal arrays and high sensitivity at large scale.

The right-hand panel of Fig. 16 shows the SNR including the foreground contamination except removed apparent 1000 point sources. Because the error is proportional to $\sqrt{C_l^{FG}}$, we need a 99.95 per cent reduction of the foregrounds in units of Kelvin to achieve the SNR ~ 1 with $f_{sky} = 0.5$. Large f_{sky} can reduce the required precision of the foreground removal. Thus, instruments that are capable of observing with the large FoV, have advantage. For example, the instantaneous FoV of the MWA is 100 times larger than the SKA1_LOW, and the required accuracy of foreground removal is 10 times lower than that of the SKA1_LOW. In practice, the drift scan strategy with high sensitivity can compensate for the disadvantage.

The 21 cm APS is also a source of the error term. As discussed in Adshead & Furlanetto (2008), the severity of the error term depends on the correlation coefficient. Ignoring other error terms, the SNR is approximately given by $SNR^2 \approx r_{21,D}^2 \Delta l (2l + 1) f_{sky} C_l^D / C_l^{CMB}$, where $r_{21,D}$ is cross-correlation coefficient between 21 cm line signal and the Doppler anisotropy and C_l^D is the APS of the Doppler contribution. Let us assume $C_l^D / C_l^{CMB} \approx 1/3000$, $\Delta l = 200$ at $l = 100$ and the 21 cm line, and the Doppler anisotropy are correlate
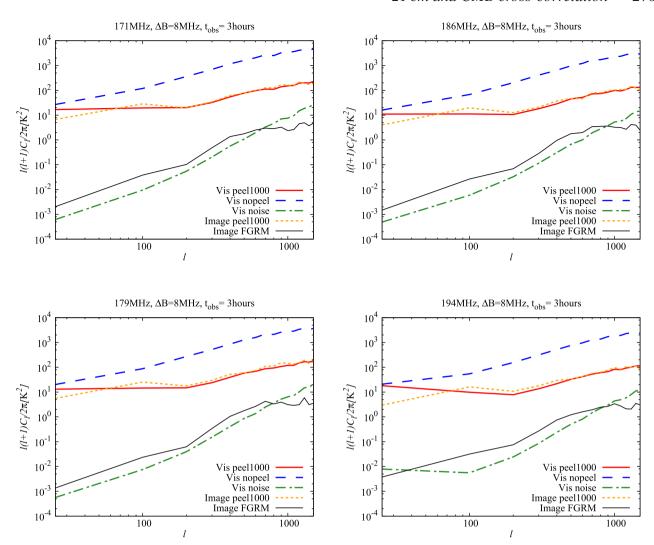
Figure 11. Comparison of the APS. Thick solid line shows the APS of visibility with peeling of 1000 point sources. The dashed line is also the APS of visibility without peeling. The dot–dashed line is the noise level estimated from the visibility data. The APS of our main images is shown as dotted line. The thin solid line is calculated from the foreground removed images described in Section 4.
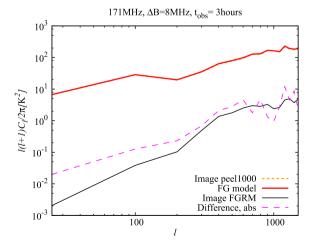

Figure 12. Comparison of the APS of our main images (dotted line) and the APS of a foreground model obtained by the polynomial fitting (thick solid line) at 171 MHz. The dashed line is the absolute value of the difference between the dotted and solid lines.

perfectly, $r_{21,D} = 1$. Although the assumption is optimistic, the f_{sky} must be larger than 0.7 to achieve the detection with high significance (SNR > 3). This pessimistic situation is improved at high-z for the early reionization model as the fraction between C_l^D and C_l^{cmb} could increase (Adshead & Furlanetto 2008).

The expected 21 cm-CMB CPS tends to be powerful at higher redshift. For example, the CPS can be $10^4\,\mu K^2$ at $z \sim 10$ for the early reionization model (e.g. Alvarez 2016). If the spectral index of the foreground and thermal noise are -2.6, the error at $z = 10$ is 2 times larger than the error at 171 MHz. Thus, the required survey area, the observation time and the precision of foreground removal are small. The analysis using lower frequency data is our future work, and it could be used to constrain the extreme reionization model.

8 SUMMARY

In this work, we have presented a first attempt to calculate the CPS between 21 cm line signal and the CMB using the 3 h of MWA data and the CMB temperature map observed by the *Planck*. For reducing the error, dominated by the foregrounds, we have subtracted 1000
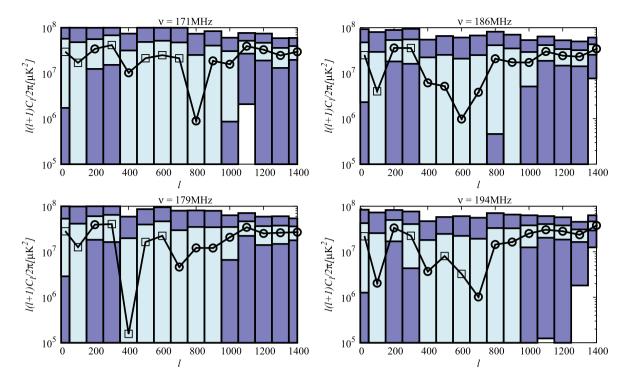
Figure 13. CPS between the MWA observed image with point source subtraction and the Planck CMB image. Black solid line is the CPS, circles indicate positive values and squares indicate negative. Boxes are the expected 1σ and 3σ error, which are calculated using equation (6). Where the boxes meet the x-axis, the signal is consistent with zero. At $l < 1000$, there are no significant detections. At small scales, unexpected signals are detected with high-significance and positive correlation.

Table 1. List of the CPS of 21 cm-CMB and 1σ error at different scales and frequencies. Using the RTS, 1000 point sources have been removed.

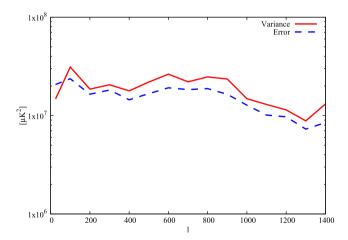|	$l = 100$	$l = 200$	$l = 500$	$l = 1000$
171 MHz	$-1.696 \times 10^7 \pm 3.117 \times 10^7$	$3.423 \times 10^7 \pm 2.181 \times 10^7$	$-2.135 \times 10^7 \pm 2.731 \times 10^7$	$1.575 \times 10^7 \pm 1.289 \times 10^7$
179 MHz	$-1.262 \times 10^7 \pm 2.885 \times 10^7$	$3.943 \times 10^7 \pm 2.107 \times 10^7$	$-1.642 \times 10^7 \pm 2.334 \times 10^7$	$2.083 \times 10^7 \pm 1.420 \times 10^7$
186 MHz	$-4.004 \times 10^6 \pm 2.545 \times 10^7$	$3.589 \times 10^7 \pm 1.777 \times 10^7$	$5.164 \times 10^6 \pm 2.018 \times 10^7$	$1.720 \times 10^7 \pm 1.209 \times 10^7$
194 MHz	$2.044 \times 10^6 \pm 2.367 \times 10^7$	$3.345 \times 10^7 \pm 1.648 \times 10^7$	$-8.054 \times 10^6 \pm 1.670 \times 10^7$	$2.526 \times 10^7 \pm 1.275 \times 10^7$

Figure 14. Comparison of the error at 194 MHz. The solid line is the variance of the CPS and the dashed line is error estimated by equation (6). For estimating the variance, we calculate the CPS between the MWA image and 100 random CMB maps.

point sources with the RTS and have removed spectrally smooth foregrounds by a polynomial fitting across frequency channels.

The 21 cm observation with the interferometers is complicated due to Earth's ionosphere, observation pointing, and foreground and frequency dependence. Thus, we have investigated the systematic contamination to the CPS. We could not find any correlation of results with level of ionospheric activity, or a dependency on frequency, but the CPS is dominated by the foreground error depending on the group of pointings. However, we have used only 3 h of data for the analysis. In future work, a larger amount of data is required.

By computing the APS using the image and visibility, we found that the Galactic foreground and point sources dominate the signal at large, $l \sim 100$, and small scales, $l > 200$. Although the simple polynomial fitting can reduce about 90 per cent of foreground, the residual was larger than the noise level.

The CPS can statistically reduce the foreground contamination. However, the extremely bright foregrounds provided a large error on the CPS, even if we removed the foregrounds. Thus, we could not detect the 21 cm-CMB signal and obtained at 68 per cent confidence interval of $\Delta C_l = 3.1 \times 10^7$ at $l = 100$ and at 171 MHz without the polynomial foreground removal. Furthermore, the variance of the
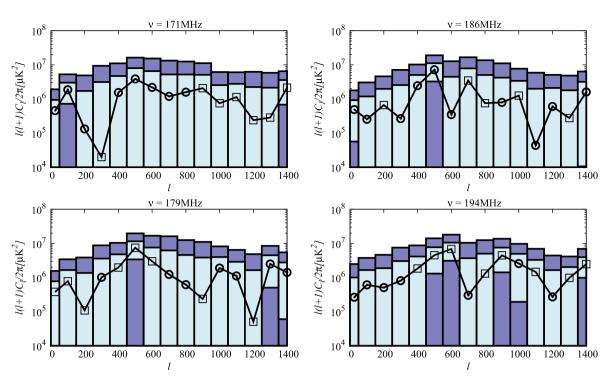
Figure 15. Same as Fig. 13, but the foregrounds are removed by the polynomial fitting with $n = 7$. There are no significant detections even at $l > 1000$.

Table 2. Same as Table 1, but we remove the foregrounds from the MWA data by the polynomial fitting method.

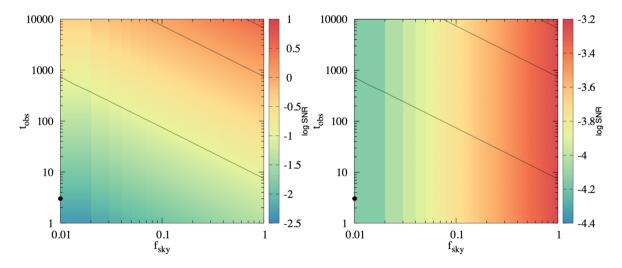|	$l = 100$	$l = 200$	$l = 500$	$l = 1000$
171 MHz	$1.864 \times 10^6 \pm 1.141 \times 10^6$	$1.325 \times 10^5 \pm 1.586 \times 10^6$	$3.875 \times 10^6 \pm 4.134 \times 10^6$	$-7.488 \times 10^5 \pm 1.800 \times 10^6$
179 MHz	$-7.779 \times 10^5 \pm 8.806 \times 10^5$	$-1.088 \times 10^5 \pm 1.253 \times 10^6$	$-7.466 \times 10^6 \pm 4.064 \times 10^6$	$1.893 \times 10^6 \pm 2.089 \times 10^6$
186 MHz	$2.546 \times 10^5 \pm 9.343 \times 10^5$	$-6.634 \times 10^5 \pm 1.313 \times 10^6$	$7.203 \times 10^6 \pm 3.944 \times 10^6$	$-1.253 \times 10^6 \pm 2.149 \times 10^6$
194 MHz	$6.090 \times 10^5 \pm 1.049 \times 10^6$	$5.070 \times 10^5 \pm 1.377 \times 10^6$	$-4.504 \times 10^6 \pm 3.198 \times 10^6$	$2.573 \times 10^6 \pm 2.379 \times 10^6$

Figure 16. Expected SNR at $l = 100$. The foreground is ignored (included) in left-hand (right-hand) panel. The three solid lines indicate that the SNR, without foreground contamination, are 0.1, 1, and 3 from bottom to top. We assume the 21 cm-CMB CPS is $10^3 \; \mu K^2$. The error is estimated from equation (6) with $\Delta l = 100$. Black point indicates SNR of this work. In the right-hand panel, the value of $\log SNR = -4$ indicates that one has to remove the 99.99 per cent of foregrounds in units of Kelvin to detect the signal.

CPS is large than the expected error due to unexpected systematics at small scales. We also have found that the measurement of CPS requires at least 50 per cent of sky fraction, 2000 h of observation time for the MWA FoV and removal of 99.95 per cent foreground in Kelvin.

REFERENCES

Adshead P. J., Furlanetto S. R., 2008, MNRAS, 384, 291
Ali Z. S. et al., 2015, ApJ, 809, 61
Alvarez M. A., 2016, ApJ, 824, 118
Alvarez M. A., Komatsu E., Doré O., Shapiro P. R., 2006, ApJ, 647, 840
Beardsley A. P. et al., 2016, ApJ, 833, 102
Bowman J. D. et al., 2013, PASA, 30, e031
Chiang H. C. et al., 2010, ApJ, 711, 1123
Chon G., Challinor A., Prunet S., Hivon E., Szapudi I., 2004, MNRAS, 350, 914
Cooray A., 2004, Phys. Rev., 70, 063509
Datta K. K., Choudhury T. R., Bharadwaj S., 2007, MNRAS, 378, 119
DeBoer D. R., 2016, Electromagnetics in Advanced Applications (ICEAA), 2016 International Conference on, 7731446
Dillon J. S. et al., 2015, Phys. Rev., 91, 123011
Dunkley J. et al., 2009, AIP Conf. Proc. Vol. 1141, CMB POLARIZATION WORKSHOP: THEORY AND FOREGROUNDS: CMBPol Mission Concept Study. Am. Inst. Phys., New York, p. 222
Fan X. et al., 2006, AJ, 132, 117
Górski K. M., Hivon E., Banday A. J., Wandelt B. D., Hansen F. K., Reinecke M., Bartelmann M., 2005, ApJ, 622, 759
Greig B., Mesinger A., 2015, MNRAS, 449, 4246
Hurley-Walker N. et al., 2017, MNRAS, 464, 1146
Hutter A., Dayal P., Müller V., Trott C. M., 2017, ApJ, 836, 176
Jacobs D. C. et al., 2015, ApJ, 801, 51
Jacobs D. C. et al., 2016, ApJ, 825, 114
Jelić V. et al., 2010, MNRAS, 402, 2279
Jordan C. H. et al., 2017, MNRAS, 471, 3974
Knox L., 1995, Phys. Rev., 52, 4307
Kubota K. et al., 2017, MNRAS, 479, 2754
Lidz A., Zahn O., Furlanetto S. R., McQuinn M., Hernquist L., Zaldarriaga M., 2009, ApJ, 690, 252
Line J. L. B., Webster R. L., Pindor B., Mitchell D. A., Trott C. M., 2017, PASA, 34, e003
Ma Q., Helgason K., Komatsu E., Ciardi B., Ferrara A., 2018, MNRAS, 476, 4025
Mellema G. et al., 2013, Exp. Astron., 36, 235
Mitchell D. A., Greenhill L. J., Wayth R. B., Sault R. J., Lonsdale C. J., Cappallo R. J., Morales M. F., Ord S. M., 2008, IEEE J. Sel. Top. Signal Process., 2, 707
Morales M. F., Hazelton B., Sullivan I., Beardsley A., 2012, ApJ, 752, 137
Neben A. R. et al., 2015, Radio Sci., 50, 614
Offringa A. R., de Bruyn A. G., Biehl M., Zaroubi S., Bernardi G., Pandey V. N., 2010, MNRAS, 405, 155
Offringa A. R. et al., 2015, PASA, 32, e008
Ord S. M. et al., 2010, PASP, 122, 1353
Ostriker J. P., Vishniac E. T., 1986, ApJ, 306, L51
Ouchi M. et al., 2010, ApJ, 723, 869
Paciga G. et al., 2013, MNRAS, 433, 639
Parsons A. R. et al., 2010, AJ, 139, 1468
Parsons A. R. et al., 2014, ApJ, 788, 106
Patil A. H. et al., 2017, ApJ, 838, 65
Planck Collaboration et al., 2016, A&A, 594, A11
Planck Collaboration et al., 2016, A&A, 596, A108
Pober J. C. et al., 2016, ApJ, 819, 8
Salvaterra R., Ciardi B., Ferrara A., Baccigalupi C., 2005, MNRAS, 360, 1063
Tashiro H., Aghanim N., Langer M., Douspis M., Zaroubi S., Jelic V., 2010, MNRAS, 402, 2617
Tingay S. J. et al., 2013, PASA, 30, e007
Trott C. M., Wayth R. B., Tingay S. J., 2012, ApJ, 757, 101
Trott C. M. et al., 2016, ApJ, 818, 139
van Haarlem M. P. et al., 2013, A&A, 556, A2
Yoshiura S., Line J. L. B., Kubota K., Hasegawa K., Takahashi K., 2017, MNRAS, 479, 2767

APPENDIX: WEIGHT CORRECTION

The image used in this work is provided with the natural weight to increase the sensitivity at large scales. Thus, the APS and CPS calculated from images are affected by the weight caused from UV-coverage. The output image can be approximately described as

$$I_i(\boldsymbol{l}) = \int U_i(\boldsymbol{u})V(\boldsymbol{u})\exp(2\pi i\boldsymbol{l}\cdot\boldsymbol{u})d^2u, \tag{A1}$$

where U is weight due to the UV-samplings and we ignore the w-term for simplicity. The main images are obtained as the average of different images, which is written as

$$
\begin{aligned}
I_{\mathrm{sum}}(\boldsymbol{l}) &= \frac{1}{N}\sum_i I_i \\
&= \frac{1}{N}\sum_i \int U_i(\boldsymbol{u})V(\boldsymbol{u})\exp(2\pi i\boldsymbol{l}\cdot\boldsymbol{u})d^2u \\
&= \int \tilde{U}(\boldsymbol{u})V(\boldsymbol{u})\exp(2\pi i\boldsymbol{l}\cdot\boldsymbol{u})d^2u,
\end{aligned}
\tag{A2}
$$

where

$$\tilde{U}(\boldsymbol{u}) = \frac{1}{N}\sum_i U_i(\boldsymbol{u}). \tag{A3}$$

Furthermore, we assume the $V(\boldsymbol{u})$ is consistent with all observations. Under the flat sky approximation, the integrated visibility is

$$V_{\mathrm{sum}} = \int I_{\mathrm{sum}}\exp(-2\pi i\boldsymbol{l}\cdot\boldsymbol{u})d^2l = \tilde{U}V, \tag{A4}$$

and the power spectrum is given by

$$C_{l,w}(\boldsymbol{u}) \propto |V_{\mathrm{sum}}^2| = \tilde{U}^2 V^2. \tag{A5}$$

By averaging over the *UV*-cells contributing to that *l*-mode ($l = 2\pi |\boldsymbol{u}|$), the APS is

$$C_{l,w}(|\boldsymbol{u}|) \propto \frac{1}{m} \sum_{|\boldsymbol{u}|}^{m} \tilde{U}^2 V^2. \tag{A6}$$

Finally, the correction for the APS can be written as

$$C_l(|\boldsymbol{u}|) \propto \frac{C_{l,w}(|\boldsymbol{u}|)}{\frac{1}{m} \sum_{|\boldsymbol{u}|}^{m} \tilde{U}^2}. \tag{A7}$$

Similarly, the correction for the CPS is given as

$$C_l^X(|\boldsymbol{u}|) \propto \frac{C_{l,w}^X(|\boldsymbol{u}|)}{\frac{1}{m} \sum_{|\boldsymbol{u}|}^{m} \tilde{U}}. \tag{A8}$$

Note that the *U* is not squared since the CMB image has no effect from the UV-samplings. To consider the error propagation, the error of the observed CPS is estimated as

$$\sigma_X^2 = \frac{1}{(2l+1)f_{\text{sky}}\Delta l} C_{l,w}^{\text{MWA}} C_l^{\text{CMB}} \left(\frac{1}{m} \sum_{|\boldsymbol{u}|}^{m} \tilde{U} \right)^{-2}, \tag{A9}$$

where $C_{l,w}^{\text{MWA}}$ is the APS of weighted image. Although our correction of the weight is simple, the image APS can reproduce the APS computed from visibility.

This paper has been typeset from a TEX/LATEX file prepared by the author.